

# Extraction of depth-dependent signals from time-resolved reflectance in layered turbid media

**Chie Sato**

**Miho Shimada**

Tokyo Institute of Psychiatry  
Department of Integrated Neuroscience  
2-1-8 Kamikitazawa, Setagaya-ku  
Tokyo 156-8585, Japan  
E-mail: chies@prit.go.jp

**Yukio Yamada**

University of Electro-Communications  
Department of Mechanical Engineering  
and Intelligent Systems  
1-5-1 Chofugaoka, Chofu  
Tokyo 182-8585, Japan  
and  
National Institute of Advanced Industrial Science  
and Technology  
Institute for Human Science and Biomedical  
Engineering  
1-2-1 Namiki, Tsukuba  
Ibaraki 305-8564, Japan

**Yoko Hoshi**

Tokyo Institute of Psychiatry  
Department of Integrated Neuroscience  
2-1-8 Kamikitazawa, Setagaya-ku  
Tokyo 156-8585, Japan

**Abstract.** We try a new approach with near-IR time-resolved spectroscopy, to separate optical signals originated in the upper layer from those in the lower layer and to selectively determine the absorption coefficient ( $\mu_a$ ) of each layer in a two-layered turbid medium. The difference curve in the temporal profiles of light attenuation between a target and a reference medium is divided into segments along the time axis, and a slope of each segment is calculated to determine the depth-dependent  $\mu_a$ . The depth-dependent  $\mu_a$  values are estimated under various conditions in which  $\mu_a$  and the reduced scattering coefficient ( $\mu'_s$ ) of each layer are changed with a Monte Carlo simulation and in phantom experiments. Temporal variation of them represents the difference in  $\mu_a$  between two layers when  $\mu'_s$  of a reference is the same as that of the upper layer of the target. The discrepancies between calculated  $\mu_a$  and the real  $\mu_a$  depend on the ratio of the real  $\mu_a$  of the upper layer to that of the lower layer, and our approach enables us to estimate the ratio of  $\mu_a$  between the two layers. These results suggest the potential that  $\mu_a$  of the lower layer can be determined by our procedure. © 2005 Society of Photo-Optical Instrumentation Engineers. [DOI: 10.1117/1.2136312]

**Keywords:** near-infrared spectroscopy; time-resolved spectroscopy; layered media; absorption coefficient; Monte Carlo simulation; phantom experiment.

Paper 05061R received Mar. 4, 2005; revised manuscript received Jul. 7, 2005; accepted for publication Jul. 15, 2005; published online Dec. 8, 2005.

## 1 Introduction

Near-infrared spectroscopy (NIRS) has often been used for noninvasive evaluation of tissue oxygenation. Recently, this technique has been developed as a tool for human brain mapping by measuring the hemodynamic changes of cerebral cortex associated with neuronal activation.<sup>1-3</sup> NIRS has some advantages over other methods for cerebral hemodynamics evaluation such as positron emission tomography (PET) and functional magnetic resonance imaging (fMRI) in terms of, for example, temporal resolution, easier handling, and less motion restriction during measurement. Some problems, however, remain to be solved before the application of NIRS to measurements of the human head. The head is a layered structure consisting of cerebral and extracerebral tissues (scalp, skull, and cerebrospinal fluid), and each layer has different optical properties. When light is applied to the scalp and diffusely reflected light is collected at a position on the scalp a few centimeters away from the incident point, the detected light carries information concerning not only the cerebral but also extracerebral tissues. Because the changes in extracerebral blood flow influence the determination of cerebral hemoglobin (Hb) concentration changes, some reports<sup>4-6</sup> have questioned the validity of cerebral NIRS. It is thus necessary to separate signals originating in the cerebral tissue from

those in the extracerebral tissue. As one of the ways for this purpose, a multidetector system consisting of continuous-wave-type (cw-type) instruments has been developed.<sup>7,8</sup> In this approach, however, separation of NIR signals attributed to cerebral and extracerebral tissues was incomplete because the measurement by different distances of light guide pairs might cause a discrepancy in the position where signals originate. In addition, with instruments of this type, it was difficult to quantify the Hb concentration.<sup>9,10</sup> The absolute value of Hb concentration is indispensable because neuronal activation and hemodynamic changes seem to significantly depend on the baseline conditions,<sup>11,12</sup> and also to compare the magnitude of the changes between different cortical areas and/or individuals.

In contrast, time-resolved reflectance measurement with short-pulsed light [time-resolved spectroscopy (TRS)], which gives a temporal profile of detected light intensity, has high potential to overcome these issues. It is believed to carry information about depth-dependent attenuation based on the correlation of detection time to penetration depth of photons.<sup>13-17</sup> Furthermore, it makes possible the determination of the optical properties in turbid media such as the absorption coefficient<sup>18,19</sup> ( $\mu_a$ ) of which acquisition at multiple wavelengths can give quantitative Hb concentrations. In most cases of conventional TRS measurements for the human head,  $\mu_a$  was determined by fitting an analytical solution of the

Address all correspondence to Chie Sato, 2-1-8 Kamikitazawa, Setagaya-ku, Tokyo 156-8585, Japan. Tel: +81-3-3304-5701. Fax: +81-3-3329-8035. E-mail: chies@prit.go.jp

photon diffusion equation for a homogenous medium to the time-resolved reflectance profile on the assumption that the target medium is a semiinfinite homogeneous. The analysis based on this assumption not only causes an error in estimation of the optical properties of the human head<sup>20–24</sup> but also cannot bring out the depth-dependent information. Therefore, new analytical methods that are suitable for layered media are required. To overcome this problem, some methods have been provided, such as by multilayered (time-dependent) diffusion equation<sup>9,25–27</sup> and by moments of distribution of time of flight.<sup>16,28</sup> Most of these analyses are employed by combination with the measurements at two or more distances, whereas a single-distance measurement is more favorable for practical measurements on the head due to the heterogeneity of the superficial layer and its curvature. On the other hand, the analysis with time-dependent mean partial path length by Steinbrink et al.<sup>16</sup> could be applied to a single-distance measurement, but it did not enable us to estimate  $\mu_a$  in a given condition but only the change in  $\mu_a$  from one condition to another.

In this paper, we attempt to develop a simple analytical method to separate optical signals originated in shallower layers from those in deeper layers and to selectively determine the  $\mu_a$  values of them by TRS measurements with a single fixed source-detector spacing. As the first step of an analysis of a multilayer model such as the human head, a two-layered medium was considered. Our approach to this purpose is “time-segment analysis,” which divides the temporal profile of detected light intensity into time segments (e.g., every 500 ps), leading to an estimation of depth dependent  $\mu_a$ . In this paper, we first demonstrate  $\mu_a$  estimated by the slope of each time segment (time-segmented  $\mu_a$ ) and its discrepancy from the real  $\mu_a$  of the lower layer under various conditions in which  $\mu_a$  and reduced scattering coefficient ( $\mu'_s$ ) of each layer were changed with a Monte Carlo simulation and in phantom experiments. We also show the relationship between such discrepancy and the difference in  $\mu_a$  between the upper and lower layers. Then we discuss a correction of time-segmented  $\mu_a$  that was estimated smaller than the real  $\mu_a$  with the ratio of time-segmented  $\mu_a$  in an earlier time segment to that in a later one. In addition, we consider a way to calculate an appropriate  $\mu_a$  in the case that  $\mu'_s$  of medium was unknown. Finally, we suggest the applicability of our approach in practical measurement.

## 2 Method for Determining $\mu_a$

### 2.1 Theoretical Consideration

When a light impulse is incident on the surface of a semiinfinite homogeneous medium (object), the time-resolved intensity of reflected light at time  $t$  can be expressed as<sup>29</sup>

$$I(t) = S(t)\exp(-\mu_a ct), \quad (1)$$

where  $\mu_a$  is the absorption coefficient of the medium,  $c$  is the light velocity in the medium, and  $S(t)$  is a scattering function that is dependent on their reduced scattering coefficient ( $\mu'_s$ ) in the photon diffusion regime. We consider a reference medium besides the object. The reflected light intensity for the reference at  $t$  is written as  $I_R(t) = S_R(t)\exp(-\mu_{a,R} ct)$ , where the subscripts  $R$  to  $I(t)$ ,  $\mu_a$ ,  $c$ , and  $S(t)$  indicate a reference.

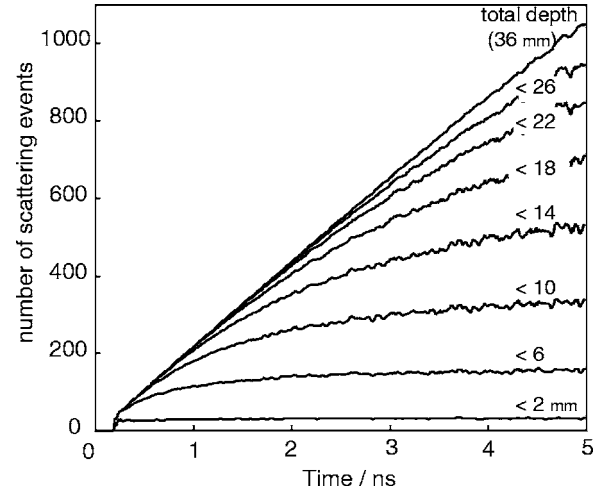


**Fig. 1** Number of scattering events in the upper part of the depth from 2 to 36 mm for a homogeneous semiinfinite medium ( $\mu_a=0 \text{ mm}^{-1}$ ,  $\mu'_s=1.0 \text{ mm}^{-1}$ ,  $\rho=30 \text{ mm}$ ,  $n=1.37$ ), predicted by Monte Carlo simulation. The vertical axis represents the number of scattering events per photon detected at time  $t$ .

Attenuation ( $A$ ) is defined as logarithm of the inverse of reflectance and according to the time-resolved Beer-Lambert law,<sup>30</sup> difference between the attenuation of an object [ $A(t)$ ] and that of a reference [ $A_R(t)$ ],  $A^{\text{diff}}(t)$ , can be expressed as

$$A^{\text{diff}}(t) = A(t) - A_R(t) = \ln[I_R(t)/I(t)] = (\mu_a c - \mu_{a,R} c) t + S^{\text{diff}}(t), \quad (2)$$

where  $S^{\text{diff}}(t) = \ln[S_R(t)/S(t)]$ . When  $\mu'_s$  and the refractive index are the same for the reference and the object,  $S^{\text{diff}}(t)$  vanishes and  $A^{\text{diff}}(t)$  becomes linear to  $t$  and its slope is denoted as  $\mu_a^{\text{diff}} c$ , where  $\mu_a^{\text{diff}} = \mu_a - \mu_{a,R}$ , and  $c = c_R$ .

However, in the case where the object is an inhomogeneous medium (and the reference is a homogeneous one),  $A^{\text{diff}}(t)$  is no longer linear to  $t$  even if  $S^{\text{diff}}(t)$  can be ignored. When  $\mu_a^{\text{diff}}$  varies due to the layer structure,  $dA^{\text{diff}}(t)/dt$  reflects the depth dependence in  $\mu_a^{\text{diff}}$ . Here we introduce time-dependent apparent absorption coefficient,  $\mu_a(t)$ , given by  $\sum_i \mu_{a,i} l_i(t)/L(t)$ , where the subscript  $i$  refers to the layer number in the object medium,  $l_i(t)$  is the mean partial path length in the  $i$ 'th layer for the photons detected at time  $t$ , and  $L(t)$  is total path length defined as  $L(t) = ct$ . Then we define time dependent difference in apparent absorption coefficient  $\mu_a^{\text{diff}}(t)$ , which is the difference between  $\mu_a(t)$  and  $\mu_{a,R}$  at each time. In the case of two-layered media, the  $i$ 'th layer simply corresponds to either upper or lower layer and  $dA^{\text{diff}}(t)/dt$  is expressed as follows:

$$\begin{aligned} dA^{\text{diff}}(t)/dt &= (d/dt)[\mu_a^{\text{diff}}(t) ct] + dS^{\text{diff}}(t)/dt \\ &= \mu_{a,\text{upper}} [dl_{\text{upper}}(t)/dt] + \mu_{a,\text{lower}} [dl_{\text{lower}}(t)/dt] \\ &\quad - \mu_{a,R} c + dS^{\text{diff}}(t)/dt, \end{aligned} \quad (3)$$

where  $\mu_{a,\text{upper}}$  and  $\mu_{a,\text{lower}}$  are the  $\mu_a$  values of the upper and lower layer for an object, and  $l_{\text{upper}}(t)$  and  $l_{\text{lower}}(t)$  are the mean partial path length in the upper and lower layers at time  $t$ , respectively. Figure 1 shows time dependence of the num-

ber of scattering events for the photons detected by reflectance mode in the upper part of the depth from 2 to 36 mm for a homogeneous semiinfinite medium ( $\mu_a=0 \text{ mm}^{-1}$ ,  $\mu'_s=1.0 \text{ mm}^{-1}$ , source-detector distance  $\rho=30 \text{ mm}$ ,  $n=1.37$ ), predicted by a Monte Carlo simulation. As for photons detected later in time in the measurement of reflectance mode, the number of scattering events in shallow layers is almost constant. This is typically seen after around 3 ns in layers that are shallower than 10 mm. Because the number of scattering events is converted to the photon path length by mean free pass, the mean partial path lengths of the shallow layers can be considered constant after 3 ns. At a later time, therefore, the mean partial path length in deeper layers is dominant to the total path length.

## 2.2 Time-Segmented $\mu_a$ and Method for Obtaining $\mu_a$ of the Lower Layer

Next, we introduced mean absorption differences obtained by  $\Delta A^{\text{diff}}(t)/\Delta t$  instead of  $dA^{\text{diff}}(t)/dt$  in consideration of errors by getting the regression curve and to simplify an analysis process. For this aim, we divided the temporal profile of detected light intensity into segments to extract time-dependent  $\mu_a$  (time-segment analysis). When we assume that  $\mu'_s$  and refractive index are the same for reference and object,

$$\begin{aligned} \Delta A^{\text{diff}}(t)/\Delta t &= (1/\Delta t)(\mu_{a,\text{upper}}\Delta I_{\text{upper}}(t) \\ &\quad + \mu_{a,\text{lower}}\Delta I_{\text{lower}}(t) - \mu_{a,R}c\Delta t) \\ &= \{\mu_{a,\text{upper}}[\Delta I_{\text{upper}}(t)/\Delta L(t)] \\ &\quad + \mu_{a,\text{lower}}[\Delta I_{\text{lower}}(t)/\Delta L(t)]\}c - \mu_{a,R}c, \quad (4) \end{aligned}$$

where  $\Delta L(t)$  is total path length change, which is  $\Delta I_{\text{upper}}(t) + \Delta I_{\text{lower}}(t) = c\Delta t$ . As shown in Fig. 1, if  $\Delta I_{\text{upper}}(t)$  is negligible after 3 ns, the slopes of  $A^{\text{diff}}(t)$  against  $ct$  at later time segments converge to  $(\mu_{a,\text{lower}} - \mu_{a,R})$ . If we know  $\mu_{a,R}$ ,  $\mu_{a,\text{lower}}$  can thus be determined. We refer to  $\{\mu_{a,\text{upper}}[\Delta I_{\text{upper}}(t)/\Delta L(t)] + \mu_{a,\text{lower}}[\Delta I_{\text{lower}}(t)/\Delta L(t)]\}$  as the time-segmented  $\mu_a$ ,  $\mu_a^{\text{seg}}$ , which represents a depth-dependent absorption coefficient at each time segment. It depends on the contribution of the change in the mean partial path length to that in the total path length between two different times. Accordingly, Eq. (4) could be rewritten again as  $\Delta A^{\text{diff}}(t)/\Delta t = (\mu_a^{\text{seg}} - \mu_{a,R})c$ .

In the following, a calculation process is explained for the case of the two-layered object and homogeneous reference. First, from the two sets of data for the object and reference, we calculate  $A^{\text{diff}}(t)$  profile and divide it into segments. Then  $A^{\text{diff}}(t)$  at each time segment is approximated linear to time and its slope (time-segmented slope) is estimated by linear regression. From the time-segmented slope,  $\mu_a^{\text{seg}}$  can be obtained from  $\mu_{a,R}$  and  $c$  based on Eq. (4). In this study, time range of 500 ps was selected for the segment size considering the reliability of regression analysis of the time-segmented slope. Before calculations of  $A^{\text{diff}}(t)$ , temporal profiles of light intensity measured by TRS are deconvoluted by the pulse response of the system that can be determined in every experiment. Deconvolution can be performed by the Fourier transform, and higher frequency components over 3/4 of the maximum are eliminated as they are judged to be noise.

## 3 Simulation and Experiment

### 3.1 Monte Carlo Simulation

To analyze the light propagation and calculate the reflectance from a two-layered semiinfinite medium, we used the Monte Carlo code developed by Wang and Jacques.<sup>31</sup> The code was modified to correspond to our measurement system. The number of scattering events in layers ranging from  $z$  to  $z+2 \text{ mm}$  in depth, and reflectance for the medium were calculated with the time step of 10 ps. Source photons were perpendicularly irradiated on the surface of the semiinfinite media, and photons that were emitted from a detector position on the surface were all detected. The source-detector distance was 30 mm. The calculation was repeated until the number of the detected photons reached 1,000,000. For each layer separately,  $\mu'_s$  were given as 1.0 and 1.5  $\text{mm}^{-1}$  and  $\mu_a$  were varied at the range of 0.005 to 0.02  $\text{mm}^{-1}$ . These values were chosen close to the optical properties of the tissues in human heads,  $\mu'_s$  and  $\mu_a$  of the head<sup>32</sup> were 0.7 to 1.0 and 0.012 to 0.016  $\text{mm}^{-1}$  at 825 nm, and  $\mu'_s$  and  $\mu_a$  of gray matter<sup>33</sup> were 0.4 to 0.7 and 0.018  $\text{mm}^{-1}$  at 849 nm, respectively. To compare with the results of phantom experiments described in the following, a case for smaller  $\mu_a$  value (0.005  $\text{mm}^{-1}$ ) was also examined. We compared some reflectance profiles simulated in an anisotropic setting (scattering coefficient  $\mu_s=10 \text{ mm}^{-1}$ , anisotropy parameter  $g=0.9$ ) with those in an isotropic one ( $\mu'_s=1.0 \text{ mm}^{-1}$ ) and confirmed that the difference between the two was small enough to be ignored. Therefore, isotropic scattering was assumed to reduce the calculation time. A refractive index of 1.37 was used for both the upper and lower layers.

### 3.2 Phantom Preparation

Homogeneous and two-layered gelatin phantoms, the sizes of which were  $230 \times 230 \times 55$  to  $70 \text{ mm}$ , were prepared. The thicknesses of the upper layers in two-layered phantoms were 10 and 15 mm. The base material of phantoms was an 8 wt% gelatin (Wako Pure Chemical Industries, Ltd., Osaka, Japan) solution. The gelatin solution itself was transparent and its  $\mu_a$  is 0.003  $\text{mm}^{-1}$  at 760 nm. We adjusted  $\mu'_s$  and  $\mu_a$  to 1.0 to 1.5 and 0.003 to 0.02  $\text{mm}^{-1}$  at 760 nm, respectively, by adding Intralipid (Fresenius Kabi AB, Upsala, Sweden) as scatterers and ink (greenish brown ink; Chugai Kasei Co., Musashino, Japan;  $\mu_a$  at 760, 800, and 830 nm were 0.247, 0.180, and 0.125  $\text{mm}^{-1}$ , respectively, in 1 vol% aqueous solution) as an absorber. A homogeneous phantom without ink (S0;  $\mu'_s=1.0 \text{ mm}^{-1}$ ,  $\mu_a=0.003 \text{ mm}^{-1}$ ) was also prepared as a reference for analysis. We determined  $\mu'_s$  and  $\mu_a$  of each phantom by curve fitting the solution of photon diffusion equation to time-resolved data (the details are described in Sec. 3.4). To confirm the reproducibility of the results, we prepared eight homogeneous phantoms on different days and/or at different times and compared their optical properties. The thickness of the upper layer and optical properties of phantoms are listed in Table 1.

### 3.3 Instrumentation

A single-channel TRS instrument<sup>34</sup> (TRS-10, Hamamatsu Photonics KK, Hamamatsu, Japan) was employed in this study. In the TRS-10, three laser diodes with different wave-

**Table 1** Sets of optical properties at 760 nm of gelatin phantoms used in experiment, where  $\mu_a$  and  $\mu'_s$  are theoretical values based on the concentration of ink and Intralipid, respectively.

| Phantom Name | Optical Coefficient at 760 nm (Prepared Value)/mm <sup>-1</sup> |         |             |         |             |
|--------------|---|---------|-------------|---------|-------------|
|              | Homogeneous   |         | Upper Layer |         | Lower Layer |
|              | Thickness/mm <sup>-1</sup>                                      | $\mu_a$ | $\mu'_s$    | $\mu_a$ | $\mu'_s$    |
| S0           |   | 0.003   | 1.0         |         |             |
| S1           |   | 0.008   | 1.0         |         |             |
| L0           | 10  | 0.003   | 1.0         | 0.003   | 1.0         |
| L1           | 10,15   | 0.013   | 1.0         | 0.008   | 1.0         |
| L2           | 10,15   | 0.003   | 1.0         | 0.008   | 1.0         |
| L3           | 15  | 0.003   | 1.0         | 0.004   | 1.0         |
| L4           | 10  | 0.003   | 1.0         | 0.015   | 1.0         |
| L5           | 10  | 0.003   | 1.0         | 0.017   | 1.0         |
| L6           | 10,15   | 0.0105  | 1.0         | 0.008   | 1.0         |
| L7           | 10,15   | 0.019   | 1.0         | 0.015   | 1.0         |
| L8           | 10  | 0.003   | 1.0         | 0.008   | 1.2         |
| L9           | 10  | 0.018   | 1.0         | 0.020   | 1.2         |
| L10          | 10  | 0.003   | 1.2         | 0.004   | 1.0         |
| L11          | 10  | 0.003   | 1.2         | 0.008   | 1.0         |
| L12          | 10  | 0.013   | 1.5         | 0.008   | 1.0         |
| L13          | 10  | 0.003   | 1.2         | 0.008   | 1.2         |

lengths (760, 800, and 830 nm) generate optical light pulses having duration of around 100 ps (full width at half maximum; FWHM) at the repetition rate of 5 MHz. After adjusting the intensity by an optical attenuator, light pulses are delivered to the sample through an optical light guide [GI type, 200  $\mu$ m core diameter, numerical aperture (NA)=0.25]. The strongest power irradiated to the sample is around 30  $\mu$ W at each wavelength. The light pulses passing through the sample are collected by a fiber bundle (3 mm diameter, NA=0.21), and transmitted to a high-speed photomultiplier tube with S-25 photocathode (H6279-MOD, Hamamatsu Photonics KK, Japan) for single-photon detection in the NIR light region. A circuit for time-resolved measurement based on time-correlated single-photon counting (TCSPC) method measures the temporal profile. Minimal data acquisition time is 100 ms.

### 3.4 Time-Resolved Measurement and Determination of Optical Properties of Phantoms

In phantom experiments, as shown in Fig. 2, incident and detecting light guide with a separation of 30 mm were placed on the upper surface of a phantom. Measurements with an accumulation time of 10 s were performed at more than three

different positions within an area 40 mm apart from the edge of the phantom to avoid the distortion of photon diffusion due to the edge. The count rate was adjusted to 100 to 150 kcps at each wavelength by optical attenuator to prevent the pile-up distortion. We avoided specular reflection and light leakage by employing a black light-guide holder. In every experiment, the instrumental responses of the TRS-10 were measured, facing the input and receiving fibers each other through a neutral density filter in a black tube. The instrumental response was around 150 ps FWHM at each wavelength.

Optical properties in homogeneous phantoms and in each layer of the two-layered phantoms were determined by fitting an analytical solution of the photon diffusion equation to the measured temporal profile with nonlinear least squares regression. The data in a time range of 0 to 5400 ps were selected for fitting. In obtaining the analytical solution, the extrapolated boundary condition of reflectance mode<sup>35,36</sup> was employed. The theoretical profile was convoluted with the measured incident pulse shape in the fitting process. Light velocity in gelatin was assumed to be 0.225 mm/ps, corresponding to its refractive index of 1.33. The same values of these were also used for the calculation of  $\mu_a^{\text{seg}}$ .

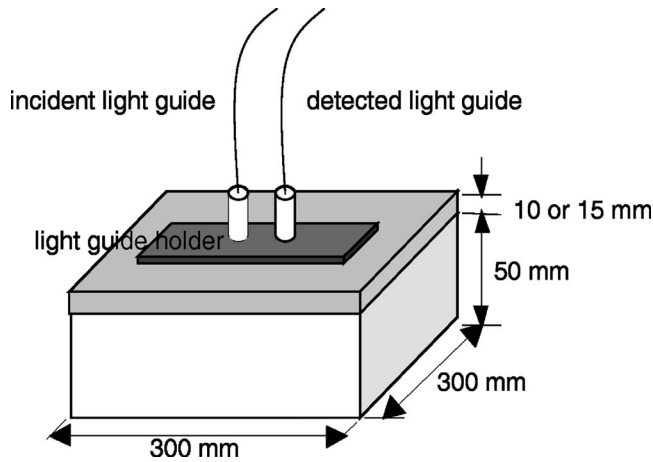


**Fig. 2** Schematic of the measurement for samples. It performed by reflectance mode, in which both light guides for radiation and detection are arranged in parallel. A mat black plate that has holes for light guides is on the samples as a light guide holder to decrease the error due to specular reflection and light leakage.

## 4 Results

### 4.1 Monte Carlo Simulation

#### 4.1.1 Temporal variations of $\mu_a^{\text{seg}}$

First we examined the temporal variations of  $\mu_a^{\text{seg}}$  under several conditions in which the  $\mu_a$  of each layer were changed. As a matter of convenience, the segments were numbered as I, II, III, etc. in order of time starting from  $t=500$  ps (e.g., the segment by time range from 500 to 1000 ps was denoted as segment I and that from 2500 to 3000 ps was as segment V, and so on). Figure 3 shows the variations of  $\mu_a^{\text{seg}}(K)$  ( $K$ =segment number) of media, the upper layer thickness of which was 10 mm and  $\mu_s'$  of both layers were  $1 \text{ mm}^{-1}$ . The  $\mu_a^{\text{seg}}(K)$  are expressed as the ratio to the real  $\mu_{a,\text{lower}}$ . A homogeneous medium was used as a reference profile ( $\mu_s' = 1 \text{ mm}^{-1}$ ,  $\mu_a = 0.005 \text{ mm}^{-1}$ ). Roughly, three types of the  $\mu_a^{\text{seg}}(K)$  curves were observed. The  $\mu_a^{\text{seg}}(K)$  in the case of the identical  $\mu_a$  between the two layers were almost constant in all the time segments. In the case where  $\mu_{a,\text{upper}}$  was larger than  $\mu_{a,\text{lower}}$ , the ratio of  $\mu_a^{\text{seg}}(K)$  to the real  $\mu_{a,\text{lower}}$  was above 1 at 0.5 to 1 ns (segment I) and gradually decreased with time, converging on 1 in 2.5 to 3.5 ns (segments V and VI). On the other hand, in the case where  $\mu_{a,\text{upper}}$  was smaller than  $\mu_{a,\text{lower}}$ ,  $\mu_a^{\text{seg}}(I)$  was below 1 at 0.5 to 2 ns and increased with time. Even in a later time period,  $\mu_a^{\text{seg}}(K)$  did not reach the  $\mu_{a,\text{lower}}$ .

#### 4.1.2 Effects of the difference in scattering on $\mu_a^{\text{seg}}$

Next, using two additional two-layered models in which upper  $\mu_s'$  was different from the lower  $\mu_s'$ , we examined the effects of the difference in  $\mu_s'$  between the two layers on the  $\mu_a^{\text{seg}}(K)$ . Figure 4(a) shows the temporal variations of  $\mu_a^{\text{seg}}(K)$  of the media with different  $\mu_s'$  between the two layers as well as those of media with the same  $\mu_s'$ . As the reference profile, a homogeneous medium in which  $\mu_s'$  was the same as that of the upper layer ( $\mu_s' = 1$  or  $1.5 \text{ mm}^{-1}$ ,  $\mu_a = 0 \text{ mm}^{-1}$ ) was used.

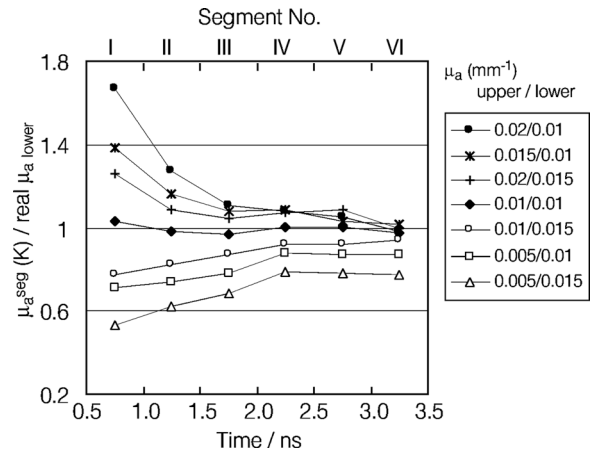


**Fig. 3** Temporal variations of  $\mu_a^{\text{seg}}(K)$  of the two-layered media, where the upper layer thickness was 10 mm and  $\mu_s'$  of both layers were  $1 \text{ mm}^{-1}$ , predicted by Monte Carlo simulation. The vertical axis represents the ratio of  $\mu_a^{\text{seg}}(K)$  to the real  $\mu_{a,\text{lower}}$ . A homogeneous medium was used as a reference profile ( $\mu_s' = 1 \text{ mm}^{-1}$ ,  $\mu_a = 0.005 \text{ mm}^{-1}$ ).

The vertical axis represents the ratio of  $\mu_a^{\text{seg}}(K)$  to the real  $\mu_{a,\text{lower}}$ . Even though upper and lower  $\mu_s'$  values were different from each other in the range from 1.0 to  $1.5 \text{ mm}^{-1}$ , the temporal variation of  $\mu_a^{\text{seg}}(K)$  was very similar to that in the case in which both layers had the same  $\mu_s'$ .

Figure 4(b) shows the effects of the  $\mu_s'$  difference between an object and a reference on the temporal variations of  $\mu_a^{\text{seg}}(K)$ . Each  $\mu_a^{\text{seg}}(K)$  was calculated by a reference in which  $\mu_s'$  was the same ( $1.0 \text{ mm}^{-1}$ ) as, larger ( $1.2 \text{ mm}^{-1}$ ) than, and smaller ( $0.8 \text{ mm}^{-1}$ ) than that of upper layer of an object. When we used a reference with larger  $\mu_s'$ ,  $\mu_a^{\text{seg}}(K)$  in the earlier time segments were larger than  $\mu_a$  estimated by a reference with the same  $\mu_s'$ . In contrast, when a reference with smaller  $\mu_s'$  was used,  $\mu_a^{\text{seg}}(I)$  was smaller than that in the case of the same  $\mu_s'$ . The  $\mu_a^{\text{seg}}(VI)$  calculated by a  $1.2\text{-mm}^{-1}$  reference and the  $\mu_a^{\text{seg}}(V)$  and (VI) by the  $0.8\text{-mm}^{-1}$  reference were almost equal to that calculated by the reference with the same  $\mu_s'$  ( $1.0 \text{ mm}^{-1}$ ).

#### 4.1.3 Effect of the $\mu_a$ difference between the upper and lower layer on the $\mu_a^{\text{seg}}$ in later segments

Figure 5 shows the  $\mu_a^{\text{seg}}(IV)$ , (V), and (VI) of two-layered media (upper layer thickness=10 mm) predicted by Monte Carlo simulation as a function of the ratio of  $\mu_{a,\text{upper}}$  to  $\mu_{a,\text{lower}}$  ( $\mu_{a,\text{ratio}}^{\text{upper/lower}}$ ). The data obtained in the cases in which  $\mu_s'$  was equal (the models in Sec. 4.1.1) and different (the models in Sec. 4.1.2) between the two layers were plotted together. As the reference profile, a homogeneous medium in which  $\mu_s'$  was the same as that of the upper layer was used. When the  $\mu_{a,\text{ratio}}^{\text{upper/lower}}$  was equal to or more than 1, the  $\mu_a^{\text{seg}}(IV)$ , (V), and (VI) nearly represented the real  $\mu_a$ . The error was less than 5.0% in segment VI. On the other hand, the  $\mu_a^{\text{seg}}(K)$  even in these later time periods were smaller than the real  $\mu_a$  in the range of the  $\mu_{a,\text{ratio}}^{\text{upper/lower}}$  less than 1. The deviation grew larger as the  $\mu_{a,\text{ratio}}^{\text{upper/lower}}$  decreased.

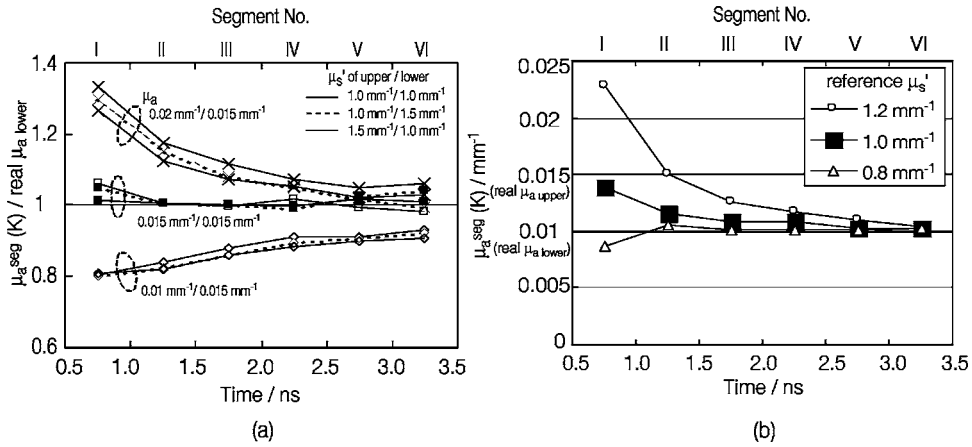


**Fig. 4** (a) Temporal variations of  $\mu_a^{\text{seg}}(K)$  of two-layered media with different  $\mu_s'$  between the two layers together with those of media with the same  $\mu_s'$  predicted by Monte Carlo simulation. The upper layer thickness was 10 mm. As a reference profile, a homogeneous medium in which  $\mu_s'$  was the same as that of the upper layer ( $\mu_s'=1$  or  $1.5 \text{ mm}^{-1}$ ,  $\mu_a=0.005 \text{ mm}^{-1}$ ) was used. The vertical axis represents the ratio of  $\mu_a^{\text{seg}}(K)$  to the real  $\mu_{a,\text{lower}}$ . (b) Temporal variations of  $\mu_a^{\text{seg}}(K)$  of two-layered media (upper layer:  $\mu_s'=1 \text{ mm}^{-1}$ ,  $\mu_a=0.015 \text{ mm}^{-1}$ , lower layer:  $\mu_s'=1 \text{ mm}^{-1}$ ,  $\mu_a=0.01 \text{ mm}^{-1}$ ; upper layer thickness=10 mm) predicted by Monte Carlo simulation and analyzed using three different homogeneous references [ $\mu_s'=0.8$  ( $\Delta$ ),  $1.0$  ( $\blacksquare$ ),  $1.2 \text{ mm}^{-1}$  ( $\circ$ );  $\mu_a=0.005 \text{ mm}^{-1}$ ].

## 4.2 Phantom Experiment

### 4.2.1 Optical properties of phantoms

Maximum deviation of the optical properties of phantoms in intra- and inter-samples from the mean value were 3 and 8%, respectively. Temporal profiles of detected light intensity in homogeneous (S0) and two-layered phantom (L0), which consists of two layers with the same optical properties as those of S0, were almost in agreement (data not shown). It was thus concluded that the effect of the interface between two layers on the pattern of photon propagation was negligible in present study conditions.

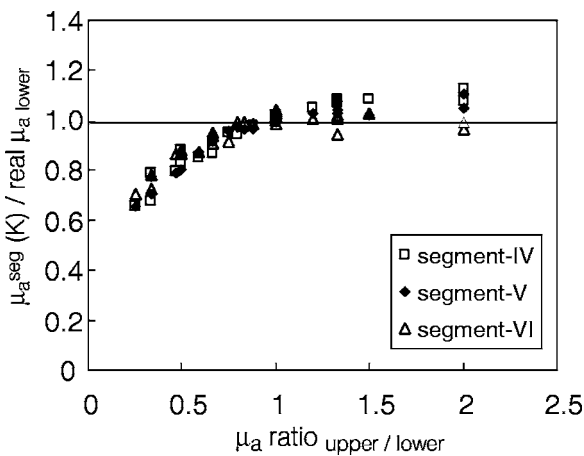


**Fig. 5** The  $\mu_a^{\text{seg}}$  (IV) ( $\square$ ), (V) ( $\blacklozenge$ ), and (VI) ( $\triangle$ ) of two-layered media predicted by Monte Carlo simulation as a function of the ratio of  $\mu_{a,\text{upper}}$  to  $\mu_{a,\text{lower}}$  ( $\mu_a \text{ ratio}_{\text{upper/lower}}$ ). Upper layer thickness was 10 mm. The data in both cases that  $\mu_s'$  was identical or different between the two layers were plotted together. A homogeneous medium in which  $\mu_s'$  was the same as that of the upper layer was used as the reference profile.

### 4.2.2 Temporal variation of $\mu_a^{\text{seg}}$

Whichever wavelength (760, 800, and 830 nm) we used, the results obtained from the following analyses of phantoms were almost the same. Thus, we present the data at 760 nm as representative results. In the phantoms with values of  $\mu_a$  larger than  $0.015 \text{ mm}^{-1}$ , the profiles of  $A^{\text{diff}}(t)$  were reliable only in the time range of 0.5 to 2 ns. Therefore, we mainly show the results of phantoms with  $\mu_a$  of 0.003 to  $0.013 \text{ mm}^{-1}$ , for which our instrument shows adequate performance, although they were smaller than that of human head generally estimated. Figure 6 shows the typical time-resolved reflectance [Fig. 6(a)] and  $A^{\text{diff}}-t$  curve [Fig. 6(b)] obtained by phantom measurements. In this condition, the data were reliable in the time period from 0.35 to 3 ns. In the early time period before 0.25 ns and in the later time period after 3 ns, data were noisy because of the interaction of incident light and/or the decrease in detected photon numbers. Therefore, analysis for slope of  $A^{\text{diff}}(t)$  (calculation of  $\mu_a^{\text{seg}}$ ) was performed in the range of 0.5 to 3 ns. The segments were numbered as I, II, III, etc. in order of time in the same manner as the case in Sec. 4.1.

Figure 7 shows temporal variations of  $\mu_a^{\text{seg}}(K)$  in two-layered phantoms (measured optical properties of L1:  $\mu_s'=1.14 \pm 0.02 \text{ mm}^{-1}$ ,  $\mu_{a,\text{upper}}=0.0143 \pm 0.0001 \text{ mm}^{-1}$ ,  $\mu_{a,\text{lower}}=0.0088 \pm 0.0002 \text{ mm}^{-1}$ ; L2:  $\mu_s'=1.12 \pm 0.01 \text{ mm}^{-1}$ ,  $\mu_{a,\text{upper}}=0.0030 \pm 0.0001 \text{ mm}^{-1}$ ,  $\mu_{a,\text{lower}}=0.0081 \pm 0.0001 \text{ mm}^{-1}$ ) with the upper layer thickness of 10 mm as well as that of the homogeneous phantom (S1:  $\mu_s'=1.06 \pm 0.02 \text{ mm}^{-1}$ ,  $\mu_a=0.0084 \pm 0.0002 \text{ mm}^{-1}$ ). The  $\mu_a^{\text{seg}}(K)$  are expressed as the ratio to the real  $\mu_{a,\text{lower}}$ . The  $\mu_s'$  of the reference was the same as that of the upper and lower layers of these phantoms. The  $\mu_a^{\text{seg}}(K)$  of S1 were almost constant in all the time segments, and the ratio to the real  $\mu_{a,\text{lower}}$  was  $0.96 \pm 0.06$ . As for L1 ( $\mu_a \text{ ratio}_{\text{upper/lower}}=1.66$ ), the ratio of  $\mu_a^{\text{seg}}(\text{I})$  to the real  $\mu_{a,\text{lower}}$  was  $1.37 \pm 0.05$ . It

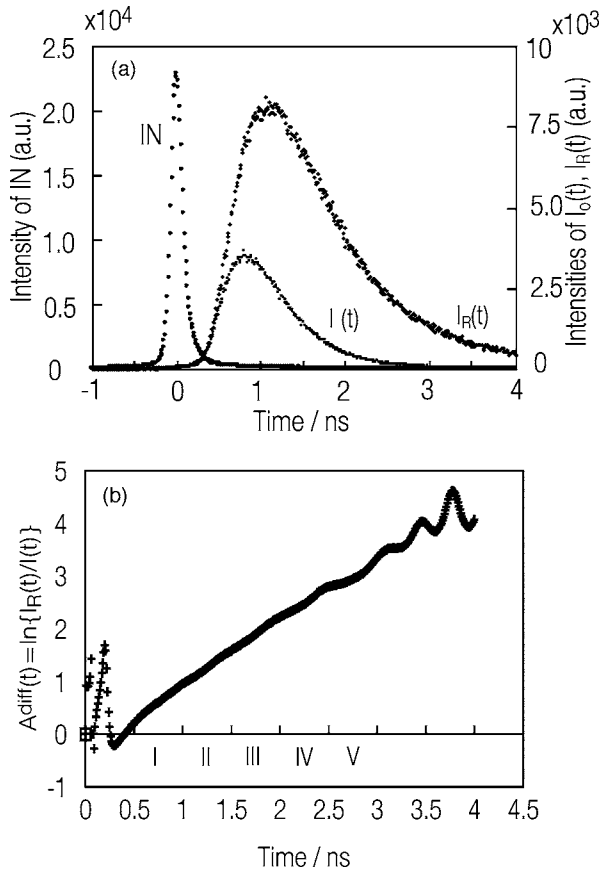


**Fig. 6** Typical time-resolved reflectance and  $A^{diff}-t$  curve obtained by phantom measurements: (a) temporal profiles of incident light (IN), intensity of the detected light through a homogeneous  $[I_R(t)]$  and a two-layered medium  $[I(t)]$  and (b)  $A^{diff}-t$  curve obtained from the data in (a) in the time period of 0 to 4 ns. The data of detected light intensity through the phantoms are deconvoluted by the temporal profile of the incident light and  $A^{diff}$  at each time was calculated. The Roman numerals show numbers of segments of the curve parted every 0.5 ns to get the  $\mu_a^{seg}$ .

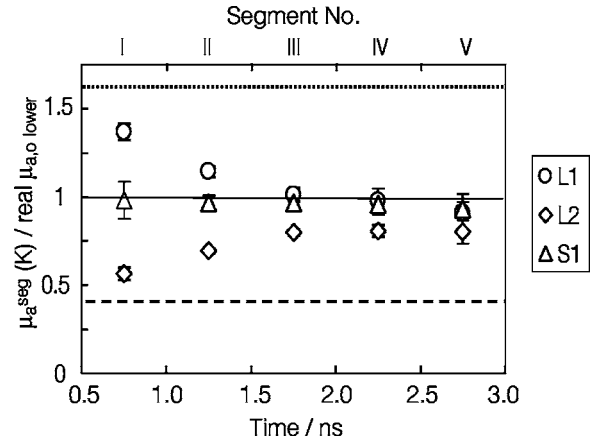
gradually decreased with time to  $0.98 \pm 0.07$  in segment IV and  $0.91 \pm 0.01$  in segment V. On the other hand, in L2 ( $\mu_a \text{ratio}_{upper/lower} = 0.40$ ),  $\mu_a^{seg}(I)$  was  $0.56 \pm 0.04$  and increased with time to  $0.80 \pm 0.05$  in  $\sim 3$  ns (segment V).

Figure 8 shows the temporal variations of  $\mu_a^{seg}(K)$  of phantoms with an upper layer thickness of 15 mm. The optical properties of each layer in L1' and L2' were the same as those of L1 and L2, respectively. For comparison,  $\mu_a^{seg}(K)$  of S1 is also shown. Like in the phantoms with an upper layer thickness of 10 mm shown in Fig. 7, the pattern of  $\mu_a^{seg}(K)$  was dependent on  $\mu_{a,upper}$ . When  $\mu_{a,upper}$  was larger than  $\mu_{a,lower}$  (L1'), the  $\mu_a^{seg}(V)$  indicated  $\mu_{a,lower}$ .

The effects of the scattering difference on the temporal variations of  $\mu_a^{seg}(K)$  were found in a similar manner to the results by Monte Carlo simulation (data not shown).

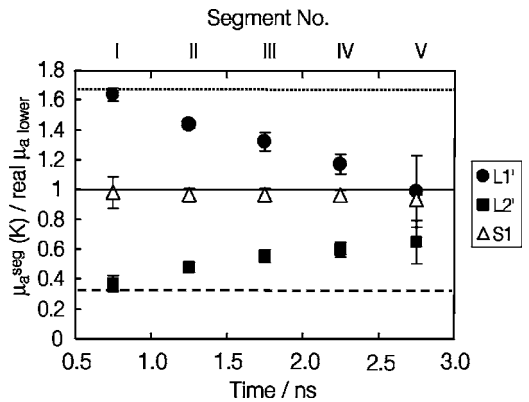
#### 4.2.3 Effect of the $\mu_a$ difference between the upper and lower layer on the $\mu_a^{seg}$ in later segments

Figure 9 shows the  $\mu_a^{seg}$  in segment IV [Fig. 9(a)] and segment V [Fig. 9(b)] as a function of  $\mu_a \text{ratio}_{upper/lower}$  by mea-



**Fig. 7** Temporal variations of  $\mu_a^{seg}(K)$  of two-layered phantoms (L1 and L2), of which upper layer thickness was 10 mm, and homogeneous phantom of S1 (L1:  $\mu'_s = 1.14 \pm 0.02 \text{ mm}^{-1}$ ,  $\mu_{a,upper} = 0.0143 \pm 0.0001 \text{ mm}^{-1}$ ,  $\mu_{a,lower} = 0.0088 \pm 0.0002 \text{ mm}^{-1}$ ; L2:  $\mu'_s = 1.12 \pm 0.01 \text{ mm}^{-1}$ ,  $\mu_{a,upper} = 0.0030 \pm 0.0001 \text{ mm}^{-1}$ ,  $\mu_{a,lower} = 0.0081 \pm 0.0001 \text{ mm}^{-1}$ ; S1:  $\mu'_s = 1.06 \pm 0.05 \text{ mm}^{-1}$ ,  $\mu_a = 0.0084 \pm 0.0002 \text{ mm}^{-1}$ ). A homogeneous phantom S0 ( $\mu'_s = 1.01 \pm 0.04 \text{ mm}^{-1}$ ,  $\mu_a = 0.0030 \pm 0.0001 \text{ mm}^{-1}$ ) was used as a reference. The plots represent mean  $\pm$ SD (standard deviation) ratio of  $\mu_a^{seg}(K)$  to the real  $\mu_{a,lower}$  (L1, L2:  $n=3$  positions  $\times 2$  samples; S1:  $n=3$  positions  $\times 8$  samples). Top dotted line and bottom broken line indicate the real  $\mu_{a,upper}$  shown as the ratio to the real  $\mu_{a,lower}$  in L1 and L2, respectively.

surements of phantoms in Table 1. As in the Monte Carlo simulation, the  $\mu_a^{seg}(K)$  in later time periods depended on the difference in  $\mu_a$  values between the upper and the lower layers: it was smaller than the real  $\mu_{a,lower}$  in the range of the  $\mu_a \text{ratio}_{upper/lower}$  less than 1, while it almost represented the real  $\mu_{a,lower}$  when the  $\mu_a \text{ratio}_{upper/lower}$  was equal to or more than 1. In the case in which upper layer thickness was 15 mm, the  $\mu_a^{seg}$  was much smaller in the range of the  $\mu_a \text{ratio}_{upper/lower}$



**Fig. 8** Temporal variations of  $\mu_a^{seg}(K)$  of two-layered phantoms (L1' and L2'), of which the upper layer thickness was 15 mm, and homogeneous phantom of S1 at 760 nm using S0 ( $\mu'_s = 1.0 \text{ mm}^{-1}$ ,  $\mu_a = 0.003 \text{ mm}^{-1}$ ) as a reference. The optical properties of each layer in L1' and L2' are the same as L1 and L2. The notation of the vertical axis is the same as that of Fig. 7. Values are means  $\pm$ SD (L1', L2':  $n=3$  positions  $\times 2$  samples, S1:  $n=3$  positions  $\times 8$  samples). Top dotted line and bottom broken line represent the real  $\mu_{a,upper}$  shown as the ratio to the real  $\mu_{a,lower}$  in L1' and L2', respectively.

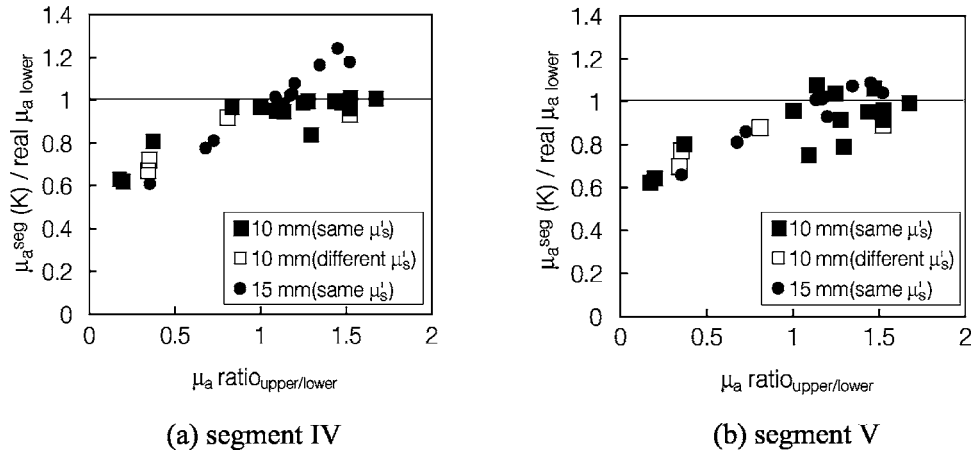


**Fig. 9** Plots of  $\mu_a^{\text{seg}}$  in (a) segment IV and (b) segment V in reference to the ratio of  $\mu_{a,\text{upper}}$  to  $\mu_{a,\text{lower}}$  ( $\mu_a \text{ ratio}_{\text{upper/lower}}$ ) of three kinds of phantoms (Table 1); upper layer thickness is 10 mm and  $\mu_s'$  of both layers are the same as the reference (■), upper layer thickness is 10 mm and  $\mu_s'$  of the lower layer is different from the reference (□), and upper layer thickness is 15 mm and  $\mu_s'$  of both layers are the same as the reference (●). The vertical axis represents the ratio of  $\mu_a^{\text{seg}}(K)$  to the real  $\mu_{a,\text{lower}}$ . Each plot was average value by several measurements for one sample.

below 1, while it was larger than the real values in the range of the  $\mu_a \text{ ratio}_{\text{upper/lower}}$  above 1 in segment IV, but not in segment V. When the  $\mu_s'$  value of the lower layer was different from that of the reference, there were no significant changes in the relationship between the  $\mu_a \text{ ratio}_{\text{upper/lower}}$  and the  $\mu_a^{\text{seg}}(\text{IV})$  or (V).

## 5 Discussion

### 5.1 Relationship Between $\mu_a^{\text{seg}}$ and Real $\mu_a$ of Each Layer

Time segment analysis, dividing the temporal profile of detected light intensity into segments, leads to some findings on path distribution in the direction of depth of photons detected at each time for layered turbid media with absorbers.

The results obtained from the analyses for Monte Carlo simulation data were generally confirmed by those of phantom experiments data. As one of the mutual results, it was found that the  $\mu_a^{\text{seg}}$  values in later segments depended on the difference in real  $\mu_a$  between two layers. This represents that in later time, the partial path length in each layer depends on both  $\mu_a$  values of the layers because the probability that the photons mainly passed in the larger  $\mu_a$  layer are detected declines. When  $\mu_{a,\text{upper}}$  is smaller than  $\mu_{a,\text{lower}}$ ,  $l_{\text{upper}}/l_{\text{lower}}$  at a later time is relatively high and  $\Delta l_{\text{upper}}$  cannot be ignored even in later time segments. Thus,  $\mu_a^{\text{seg}}$  was underestimated by the effect of  $\mu_{a,\text{upper}}$ . In contrast, when  $\mu_{a,\text{upper}}$  is equal to or larger than  $\mu_{a,\text{lower}}$ ,  $l_{\text{lower}}$  of photons detected later in time is sufficiently longer than  $l_{\text{upper}}$  and steadily increase with  $t$ , that is,  $(\Delta l_{\text{upper}}/\Delta L)$  can be considered nearly zero in later time periods, as expected. The presented results, for which  $\mu_a^{\text{seg}}$  were underestimated if  $\mu_{a,\text{upper}}$  was smaller than  $\mu_{a,\text{lower}}$ , were in agreement with a study by Hielscher et al.,<sup>22</sup> who employed a curve-fitting method with homogeneous diffusion equation to later part of the time-resolved reflectance.

Similarly,  $\mu_a^{\text{seg}}(\text{I})$  did not give the real  $\mu_{a,\text{upper}}$  values correctly, which were also affected by the difference in  $\mu_a$  between two layers (data not shown). As shown in Fig. 1, the photons detected at 500 to 1000 ps have a low probability of

passing through layers lower than the depth of 10 mm. Although  $\Delta l_{\text{upper}}$  is dominant to  $\Delta L$ ,  $\Delta l_{\text{lower}}/\Delta L$  cannot be taken as zero even in this period, especially when the thickness of the upper layer is less than 10 mm. To estimate  $\mu_{a,\text{upper}}$  more properly, it might be effective to use an earlier time segment of  $A^{\text{diff}}-t$  curve (e.g., at 350 to 700 ps). But due to the interference of incident light, it seems difficult to select the optimal time period in practical measurements.

### 5.2 Estimation of $\mu_a \text{ ratio}_{\text{upper/lower}}$ by the Ratio of $\mu_a^{\text{seg}}$ at an Early Time to that at a Later Time

In spite of the discrepancy of  $\mu_a^{\text{seg}}$  from the real  $\mu_a$ , our method gives us enough information to know the difference in  $\mu_a$  between the upper and lower layers. Moreover, based on the relationship between the extent of underestimation of  $\mu_a$  and the ratio of the real  $\mu_a$  of two layers (Fig. 5), we would derive  $\mu_{a,\text{lower}}$  by correction of  $\mu_a^{\text{seg}}$  under the condition where  $\mu_s'$  of the upper layer and that of a reference are the same and upper layer thickness is almost known. For judgment of the  $\mu_a \text{ ratio}_{\text{upper/lower}}$ , we attempted to use the  $\mu_a^{\text{seg}}$  at an early time (segment I) and at a later time (segment V) ( $\mu_a^{\text{seg}} \text{ ratio}_{\text{IV/V}}$ ). First, under the condition where  $\mu_s'$  of the reference was the same as that of the upper layer of the medium, we examined the  $\mu_a^{\text{seg}} \text{ ratio}_{\text{IV/V}}$  of various media with different  $\mu_a \text{ ratio}_{\text{upper/lower}}$  predicted by the Monte Carlo simulation. Figure 10 shows the plots of  $\mu_a \text{ ratio}_{\text{upper/lower}}$  to  $\mu_a^{\text{seg}} \text{ ratio}_{\text{IV/V}}$ . There was a strong linear correlation between these values ( $r^2=0.99$ ). Then we checked the relationship between the ratio of the  $\mu_a^{\text{seg}}(\text{V})$  to the real  $\mu_{a,\text{lower}}$  and the  $\mu_a^{\text{seg}} \text{ ratio}_{\text{IV/V}}$  for both data sets by Monte Carlo simulation [Fig. 11(a)] and by phantom experiment [Fig. 11(b)]. In the range of this ratio below 1, the  $\mu_a^{\text{seg}}(\text{V})/\mu_{a,\text{lower}}$  linearly related to the  $\mu_a^{\text{seg}} \text{ ratio}_{\text{IV/V}}$ , i.e., we could express them as  $\mu_a^{\text{seg}}(\text{V})/\mu_{a,\text{lower}} = a \times \mu_a^{\text{seg}} \text{ ratio}_{\text{IV/V}} + b$ , where  $a$  and  $b$  are constants. By regression analysis, the relationships and the correlation coefficients were  $a=0.85$ ,  $b=0.16$ , and  $r=0.80$  in the plot with Monte Carlo data, and  $a=0.84$ ,  $b=0.18$ , and  $r=0.96$  in that by the phantom experiment, which were almost in agreement. Seg-

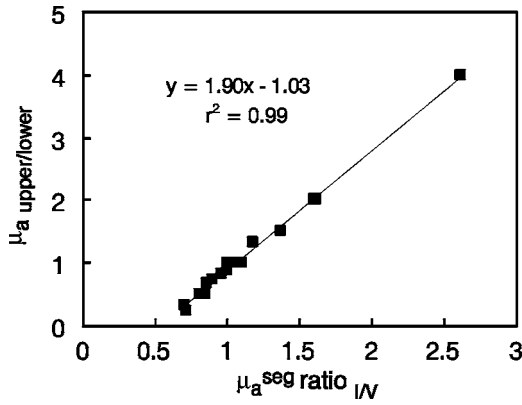


**Fig. 10** Plots of the ratio of  $\mu_{a,upper}$  to  $\mu_{a,lower}$  ( $\mu_{a,upper}/\mu_{a,lower}$ ) in reference to the ratio of  $\mu_a^{seg}(I)$  to (V) ( $\mu_a^{seg}ratio_{I/V}$ ) for the Monte Carlo simulation data.

ment IV and segment VI could also be used for the estimation of  $\mu_{a,lower}$ . But under the condition of this study, segment V was the most adequate to analyze  $\mu_{a,lower}$ , because segment IV included more information of the upper layer [cf. the case of the upper thickness of 15 mm in Fig. 9(a)] and segment VI had higher noise than segment V.

Consequently, we could evaluate  $\mu_{a,upper}/\mu_{a,lower}$  from  $\mu_a^{seg}ratio_{I/V}$  and we could estimate the  $\mu_{a,lower}$  by dividing  $\mu_a^{seg}(K)$  in later time by the value of  $(a \times \mu_a^{seg}ratio_{I/V} + b)$ . In Fig. 11, the data in both cases in which  $\mu'_s$  was equal and different between the two layers within the range of 1.0 to 1.5  $mm^{-1}$  were plotted together. Therefore, the equation for the relation between  $\mu_a^{seg}(V)/\mu_{a,lower}$  and  $\mu_a^{seg}ratio_{I/V}$  holds its validity at least under the condition that  $\mu'_s$  is 1.0 to 1.5  $mm^{-1}$  and  $\mu_a$  is 0.003 to 0.02  $mm^{-1}$  of each layer in the two-layered media.

### 5.3 Effect of the Scattering Coefficient on Estimation of $\mu_a$ of the Lower Layer

As shown in Fig. 4(a), although the  $\mu'_s$  of the lower layer was different from that of the reference, the  $\mu_a^{seg}$  values were almost identical with those for the case where the  $\mu'_s$  of the

lower layer was the same as that of the reference. In contrast, as shown in Fig. 4(b), the difference in  $\mu'_s$  between the upper layer and the reference significantly influenced the  $\mu_a^{seg}$  in earlier time segments. These results indicate that  $S^{diff}(t)$  in Eq. (2) is almost equal to the difference in scattering function only between the shallower part of the media and the reference. In addition, our results showed that the dependence of  $\mu_a^{seg}$  after 2.5 ns on the difference in  $\mu'_s$  between the upper layer and the reference was weak. These results are explained by the analytical solution derived by Patterson et al. [Eqs. (7) and (8), Ref. 18]. In the case of homogeneous media, time differential of  $S^{diff}(t)$  in Eq. (2) [or in the first line of Eq. (3)] in this paper can be represented as follows:  $dS^{diff}(t)/dt = [\rho^2/(4D_R C_R) - \rho^2/(4D_O C)]/t^2$ , where  $D_R$  and  $D_O$  are the diffusion coefficients for the reference and the object, respectively. As  $[\rho^2/(4D_R C_R) - \rho^2/(4D_O C)]$  is constant,  $dS^{diff}(t)/dt$  is in proportion to the reciprocal of the square of time. Thus, the  $dS^{diff}(t)/dt$  is negligible at the later time. Similarly, in the case of the two-layered media, it can be considered that  $dS^{diff}(t)/dt$  is very small at the later time, i.e., the effect of the  $\mu'_s$  difference on the  $\mu_a^{seg}$  at the later time segments can be negligible. In contrast, the scattering term cannot be ignored in the segment I.

### 5.4 Determination of Proper Reference with Time Segment Analysis

We have showed so far the results mainly in the case where  $\mu'_s$  of the reference was the same as that of the upper layer of the medium. However, for proper analysis with the correction in Sec. 5.2, we must select an adequate reference with  $\mu'_s$  very close to that of the upper layer of the target medium that was actually unknown. We can show one of the methods to determine the adequate reference.

As for a homogeneous medium, if  $\mu'_s$  of an object and a reference are the same, which implies  $S^{diff}(t)$  is zero in Eq. (2), the  $A^{diff}-t$  relation becomes linear. That is, if we select a reference that makes  $A^{diff}(t)$  a straight line, the  $\mu'_s$  of the reference is the same as that of the object.<sup>37</sup> In layered media, as mentioned in Sec. 5.3,  $S^{diff}(t)$  mainly depended on the difference in  $\mu'_s$  between the upper layer and the reference.

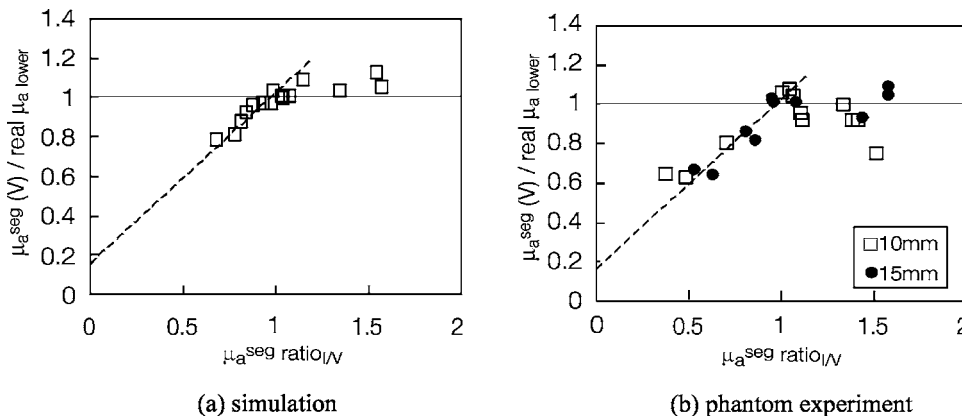


**Fig. 11** Plots of  $\mu_a^{seg}(V)$  with reference to the ratio of the  $\mu_a^{seg}(I)$  to (V) ( $\mu_a^{seg}ratio_{I/V}$ ) in (a) Monte Carlo simulation data and (b) two-layered phantoms with an upper layer thickness of 10 mm ( $\square$ ) and 15 mm ( $\bullet$ ), analyzed by a reference of which  $\mu'_s$  was the same as that of the upper layer. The vertical axis represents the ratio of  $\mu_a^{seg}(K)$  to the real  $\mu_{a,lower}$ . Broken lines are regression lines within the range of  $\mu_a^{seg}ratio_{I/V}$  below 1.

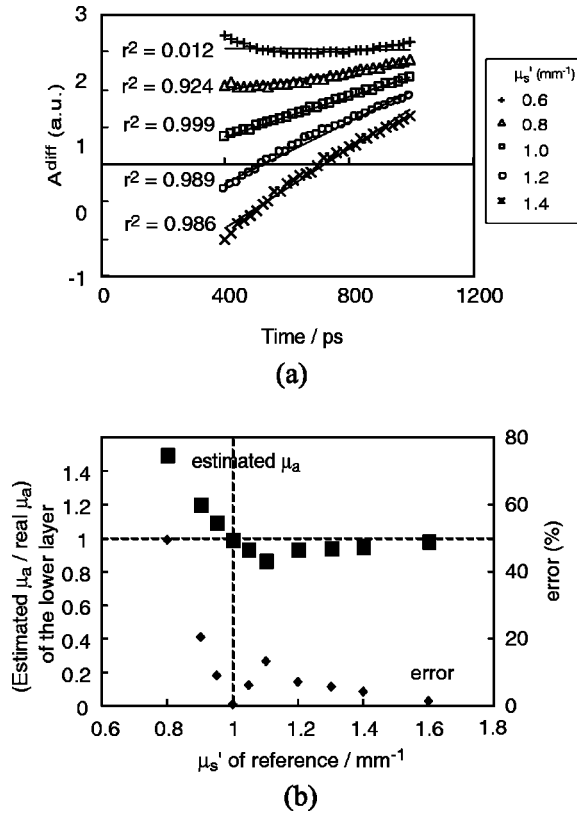


**Fig. 12** (a) The  $A^{\text{diff}}-t$  curves of a two-layered medium (upper layer:  $\mu'_s=1 \text{ mm}^{-1}$ ,  $\mu_a=0.01 \text{ mm}^{-1}$ ; and lower layer:  $\mu'_s=1.5 \text{ mm}^{-1}$ ,  $\mu_a=0.015 \text{ mm}^{-1}$ ; upper layer thickness=10 mm) in 400 to 1000 ps, predicted by Monte Carlo simulation and analyzed using five references that had various  $\mu'_s$  values within the range of 0.6 to 1.4  $\text{mm}^{-1}$  ( $\mu_a=0 \text{ mm}^{-1}$ ). (b) Estimated value of  $\mu_{a,\text{lower}}$  and the error caused by analyzing with each reference which  $\mu'_s$  was within the range of 0.8 to 1.6  $\text{mm}^{-1}$ . The correction of  $\mu_a^{\text{seg}}$  (V) with the equation in Sec. 5.2 was used to estimate these  $\mu_a$  values.

Thus, we applied the precedings concept that  $S^{\text{diff}}(t)$  is estimated based on the degree of linear relation for  $A^{\text{diff}}-t$  curve to two-layered media to select an adequate reference. Figure 12(a) shows  $A^{\text{diff}}-t$  curves of two-layered medium (upper layer,  $\mu'_s=1 \text{ mm}^{-1}$ ,  $\mu_a=0.01 \text{ mm}^{-1}$ , and lower layer,  $\mu'_s=1.5 \text{ mm}^{-1}$ ,  $\mu_a=0.015 \text{ mm}^{-1}$ , upper layer thickness = 10 mm) in 400 to 1000 ps, predicted by Monte Carlo simulation and analyzed using five references that had different  $\mu'_s$  values within the range of 0.6 to 1.4  $\text{mm}^{-1}$  ( $\mu_a=0 \text{ mm}^{-1}$ ). We examined the coefficient of determination  $r^2$  of each curve by linear regression analysis. It could be found that when a reference was used whose  $\mu'_s$  was the same as that of the upper layer of an object,  $r^2$  was extremely close to 1. It indicates that when thickness of the upper layer is larger than 10 mm, the change in  $\mu_a^{\text{diff}}(t)$  with  $t$  is so small as compared with that of  $S^{\text{diff}}(t)$  in time segment I and in time earlier than segment I. Thus, using this method of investigating linear relation for  $A^{\text{diff}}-t$  at an earlier time, we can select an appropriate reference. Figure 12(b) shows estimated  $\mu_a$  values of the lower layer and the errors for this model analyzed by various references already described. The correction of  $\mu_a^{\text{seg}}$  (V) with equation in Sec. 5.2 was used to estimate these  $\mu_a$ . It

was found that when a reference was used whose  $\mu'_s$  value was the same as that of the upper layer of an object, the estimated  $\mu_a$  was almost the same as the real  $\mu_a$ . We also found that when the difference in  $\mu'_s$  between a reference and the upper layer of an object was smaller than  $0.5 \text{ mm}^{-1}$ , the error of estimated  $\mu_a$  was less than 10%. In other words, we should prepare a series of reference in which  $\mu'_s$  were changed by every  $0.5 \text{ mm}^{-1}$  within the range of the human extracerebral tissue to estimate reliable  $\mu_a$  by this method.

### 5.5 Possibility of Applying the Present Method to Human Head Measurements

The time segment analysis of time-resolved reflectance in two-layered media enabled us to simply acquire information on the  $\mu_a$  of each layer and was implemented for a reflectance by measurement with a single source-detector distance. Moreover, we found that the estimated value of  $\mu_{a,\text{lower}}$  depended on the value of  $\mu_{a,\text{ratio upper/lower}}$ , i.e.,  $\mu_a^{\text{seg}}$  were underestimated if  $\mu_{a,\text{upper}}$  was smaller than  $\mu_{a,\text{lower}}$ , which was almost the same as the results in the case of fitting analysis for the later part of time-resolved reflectance by a solution of diffusion equations for homogeneous media.<sup>22</sup> In our method, however, the difference in  $\mu_a$  ( $\mu_{a,\text{ratio upper/lower}}$ ) can be evaluated using  $\mu_a^{\text{seg}}$  both at earlier time and at later time ( $\mu_{a,\text{ratio I/IV}}$ ).

For the adult human forehead, the total thickness of scalp and skull is<sup>28,38</sup> about 10 mm. Thus, the  $\mu_a$  of the brain may be estimated by  $\mu_a^{\text{seg}}$  (IV) to (VI) if the human head could be approximated to two-layered model. On the other hand, the human head is a multilayered structure and the scattering phenomenon must be more complex. Therefore we require further experiments with a more sophisticated model of the human head to confirm the utility and limitations of this method. For example, relation between the discrepancies of estimated  $\mu_a$  from the real  $\mu_a$  and the ratio of  $\mu_a^{\text{seg}}$  at an earlier time to that at a later time in multilayered models, and dependence of the layer thickness on the relationship should be examined. As the segment size, a time range of 500 ps was chosen in this study. For a multilayered model, however, we should evaluate the segment size to obtain better results. Moreover reliable estimation requires determining  $\mu'_s$  values of the scalp and skull, which vary with individuals and each position on the head.

## 6 Conclusion

We confirmed that the “time segment analysis” of time resolved reflectance for a two-layered media could selectively determine the values of  $\mu_{a,\text{lower}}$ . Under the condition where  $\mu'_s$  of a reference profile is the same as that of the upper layer of an object medium, this analysis enables us to estimate the deference in  $\mu_a$  between the upper and the lower layers. It was also possible to determine  $\mu_{a,\text{lower}}$  by correcting the  $\mu_a^{\text{seg}}$  with the ratio of  $\mu_a^{\text{seg}}$  in an earlier time segment and to that in a later one if we have rough knowledge of the upper layer thickness. In conclusion, the presented approach has a potential to selectively determine the value of  $\mu_a$  and to quantitatively evaluate concentrations of the Hb in human cerebral tissue.

## Acknowledgments

The authors very much appreciate the helpful discussion we had with Mr. Y. Yamashita and Dr. M. Oda at Hamamatsu Photonics KK.

## References

1. Y. Hoshi and M. Tamura, "Detection of dynamic changes in cerebral oxygenation coupled to neuronal function during mental work in man," *Neurosci. Lett.* **150**, 5–8 (1993).
2. T. Kato, A. Kamei, S. Takashima, and T. Ozaki, "Human visual cortical function during photic stimulation monitoring by means of near-infrared spectroscopy," *J. Cereb. Blood Flow Metab.* **13**(3), 516–520 (1993).
3. A. Villringer, J. Planck, C. Hock, L. Schleinkofer, and U. Dirnagl, "Near infrared spectroscopy (NIRS): a new tool to study hemodynamic changes during activation of brain function in human adults," *Neurosci. Lett.* **154**(1–2), 101–104 (1993).
4. T. J. Germon, A. E. Young, A. R. Manara, and R. J. Nelson, "Extracerebral absorption of near infrared light influences the detection of increased cerebral oxygenation monitored by near infrared spectroscopy," *J. Neurol., Neurosurg. Psychiatry* **58**(4), 477–479 (1995).
5. D. N. Harris and S. M. Bailey, "Near infrared spectroscopy in adults. Does the Invos 3100 really measure intracerebral oxygenation?" *Anaesthesia* **48**(8), 694–696 (1993).
6. H. Owen-Reece, C. E. Elwell, W. Harkness, J. Goldstone, D. T. Delpy, J. S. Wyatt, and M. Smith, "Use of near infrared spectroscopy to estimate cerebral blood flow in conscious and anaesthetized adult subjects," *Br. J. Anaesth.* **76**(1), 43–48 (1996).
7. P. W. McCormick, M. Stewart, M. G. Goetting, M. Dujovny, G. Lewis, and J. I. Ausman, "Noninvasive cerebral optical spectroscopy for monitoring cerebral oxygen delivery and hemodynamics," *Crit. Care Med.* **19**(1), 89–97 (1991).
8. T. J. Germon, P. D. Evans, N. J. Barnett, P. Wall, A. R. Manara, and R. J. Nelson, "Cerebral near infrared spectroscopy: emitter-detector separation must be increased," *Br. J. Anaesth.* **82**(6), 831–837 (1999).
9. A. Kienle, T. Glanzmann, G. Wagnière, and H. van den Bergh, "Investigation of two-layered turbid media with time-resolved reflectance," *Appl. Opt.* **37**(28), 6852–6862 (1998).
10. M. Larsson, H. Nilsson, and T. Strömberg, "In vivo determination of local skin optical properties and photon path length by use of spatially resolved diffuse reflectance with application in laser Doppler flowmetry," *Appl. Opt.* **42**(1), 124–134 (2003).
11. H. Laufs, A. Kleinschmidt, A. Beyerle, E. Eger, A. Salek-Haddadi, C. Preibisch, and K. Krakow, "EEG-correlated fMRI of human alpha activity," *Neuroimage* **19**(4), 1463–1476 (2003).
12. M. Moosmann, P. Ritter, I. Krastel, A. Brink, S. Thees, F. Blankenburg, B. Taskin, H. Obrig, and A. Villringer, "Correlates of alpha rhythm in functional magnetic resonance imaging and near infrared spectroscopy," *Neuroimage* **20**(1), 145–158 (2003).
13. S. D. Bianco, F. Martelli, and G. Zaccanti, "Penetration depth of light re-emitted by a diffusive medium: Theoretical and experimental investigation," *Phys. Med. Biol.* **47**, 4131–4144 (2002).
14. B. Montcel, R. Chabrier, and P. Poulet, "Detection of cortical activation with time-resolved diffuse optical method," *Appl. Opt.* **44**(10), 1942–1947 (2005).
15. J. Selb, J. J. Stott, M. A. Franceschini, A. G. Sorensen, and D. A. Boas, "Improved sensitivity to cerebral hemodynamics during brain activation with a time-gated optical system: analytical model and experimental validation," *J. Biomed. Opt.* **10**(1), 011013 (2005).
16. J. Steinbrink, H. Wabnitz, H. Obrig, A. Villringer, and H. Rinneberg, "Determining changes in NIR absorption using a layered model of the human head," *Phys. Med. Biol.* **46**, 879–896 (2001).
17. G. Zaccanti, D. Contini, M. Guriori, A. Ismaelli, H. Liszka, and A. Sassaroli, "Detectability of inhomogeneities within highly diffusing media," *Proc. SPIE* **2389**, 755–762 (1995).
18. M. S. Patterson, B. Chance, and B. C. Wilson, "Time resolved reflectance and transmittance for the non-invasive measurement of tissue optical properties," *Appl. Opt.* **28**(12), 2331–2336 (1989).
19. E. M. Sevick, B. Chance, J. Leigh, S. Nioka, and M. Maris, "Quantification of time- and frequency-resolved optical spectra for the de-termination of tissue oxygenation," *Anal. Biochem.* **195**, 330–351 (1991).
20. F. Fabbri, A. Sassaroli, M. E. Henry and S. Fantini, "Optical measurements of absorption changes in two-layered diffusive media," *Phys. Med. Biol.* **49**, 1183–1201 (2004).
21. T. J. Farrell, M. S. Patterson, and M. Essenpreis, "Influence of layered tissue architecture on estimates of tissue optical properties obtained from spatially resolved diffuse reflectometry," *Appl. Opt.* **37**(10), 1958–1972 (1998).
22. A. H. Hielscher, H. Liu, B. Chance, F. K. Tittel, and S. L. Jacques, "Time-resolved photon emission from layered turbid media," *Appl. Opt.* **35**, 719–728 (1996).
23. R. J. Hunter, M. S. Patterson, T. J. Farrell, and J. E. Hayward, "Haemoglobin oxygenation of a two-layer tissue-simulating phantom from time-resolved reflectance: effect of top layer thickness," *Phys. Med. Biol.* **47**(2), 193–208 (2002).
24. A. Kienle, M. S. Patterson, N. Dögnitz, R. Bays, G. Wagnières, and H. van den Bergh, "Noninvasive determination of the optical properties of two-layered turbid media," *Appl. Opt.* **37**, 779–791 (1998).
25. A. Kienle and T. Glanzmann, "In vivo determination of the optical properties of muscle with time-resolved reflectance using a layered model," *Phys. Med. Biol.* **44**, 2689–2702 (1999).
26. F. Martelli, A. Sassaroli, Y. Yamada, and G. Zaccanti, "Analytical approximate solutions of the time-domain diffusion equation in layered slabs," *J. Opt. Soc. Am. A* **19**(1), 71–80 (2002).
27. F. Martelli, S. Del Bianco, G. Zaccanti, A. Pifferi, A. Torricelli, A. Bassi, P. Taroni, and R. Cubeddu, "Phantom validation and in vivo application of an inversion procedure for retrieving the optical properties of diffusive layered media from time-resolved reflectance measurements," *Opt. Lett.* **29**(17), 2037–2039 (2004).
28. A. Liebert, H. Wabnitz, J. Steinbrink, H. Obrig, M. Moller, R. Macdonald, A. Villringer, and H. Rinneberg, "Time-resolved multidistance near-infrared spectroscopy of the adult head: intracerebral and extracerebral absorption changes from moments of distribution of times of flight of photons," *Appl. Opt.* **43**(15), 3037–3047 (2004).
29. K. Furutsu and Y. Yamada, "Diffusion approximation for a dissipative random medium and the applications," *Phys. Rev. E* **50**, 3634–3640 (1994).
30. Y. Nomura, O. Hazeki, and M. Tamura, "Relationship between time-resolved and non-time-resolved Beer-Lambert law in turbid media," *Phys. Med. Biol.* **42**, 1009–1022 (1997).
31. L. Wang and S. L. Jacques, "Monte Carlo modeling of light transport in multi-layered tissues in standard C," Univ. of Texas/M. D. Anderson Cancer Center, Houston (1992).
32. G. Zaccanti, A. Taddeucci, M. Barilli, P. Brusciaglioni, and F. Martelli, "Optical properties of biological tissues," *Proc. SPIE* **2389**, 513–521 (1995).
33. J. H. Choi, M. Wolf, V. Toronov, U. Wolf, C. Polzonetti, D. Hueber, L. P. Safonova, R. Gupta, A. Michalos, W. Mantulin, and E. Gratton, "Noninvasive determination of the optical properties of adult brain: near-infrared spectroscopy approach," *J. Biomed. Opt.* **9**(1), 221–219 (2004).
34. M. Oda, Y. Yamashita, T. Nakano, A. Suzuki, K. Shimizu, I. Hirano, F. Shimomura, E. Ohmae, T. Suzuki, and Y. Tsuchiya, "Nearinfrared time-resolved spectroscopy system for tissue oxygenation monitor," *Proc. SPIE* **3579**, 611–617 (1999).
35. M. S. Patterson, S. J. Madsen, J. D. Moulton, and B. C. Wilson, "Diffusion equation representation of photon migration in tissue," in *IEEE 1991 Microwave Symp. Digest*, pp. 905–908 (1991).
36. A. H. Hielscher, S. L. Jacques, L. Wang, F. K. Tittel, "The influence of boundary conditions on the accuracy of diffusion theory in time-resolved reflectance spectroscopy of biological tissues," *Phys. Med. Biol.* **40**(11), 1957–1975 (1995).
37. K. Tanaka, Y. Tanikawa, R. Araki, Y. Yamada, and E. Okada, "Measurement of optical properties of biological tissues by using time-resolved transmittance spectroscopy," *Kougaku* **31**(12), 886–892 (2002) (in Japanese).
38. H. Zhao, Y. Tanikawa, F. Gao, Y. Onodera, A. Sassaroli, K. Tanaka, and Y. Yamada, "Maps of optical differential pathlength factor of human adult forehead, somatosensory motor, occipital regions at multi-wavelengths in NIR," *Phys. Med. Biol.* **47**, 1–18 (2002).